

ISM/IGM Midterm: Parts I and III

Andrew Emerick

March 27, 2014

Below are parts I and III. I refer a lot to equations from the handouts and Draine without retyping them here. If this is annoying, let me know and I can write them out and resubmit. I did part II by hand before starting this latex file, so that is separate.

1 1 Ionization and Heating of the IGM

1.1 A

In general, detailed balance gives for both HI and HeII that,

$$n_e n_p \alpha_i(T) = n_i \Gamma \quad (1)$$

where $\alpha(T)$ is the temperature dependent recombination rate, Γ is the provided photo-ionization rate per particle, and i is either HI or HeII. At lower redshift, when the ionized fraction is large, the n_p can be taken as the total number of bound and free protons. Thus, this equation reduces to

$$x_i \Gamma_i = n_e \alpha_i(T), \quad (2)$$

as given in LF 4.20. Under the assumption that free electrons only come from ionized Hydrogen, the number density of electrons comes from

$$n_e = (1 - x_{HI}) f_H n_o (1 + z)^3, \quad (3)$$

where x_{HI} is the neutral fraction of Hydrogen, $f_H = 0.93$ is the fraction of Hydrogen in the Universe by number (f_{He} is then 0.07), and n_o is the number density of baryons given by WMAP as $n_o = 2.542 \times 10^{-7} \text{ cm}^{-3}$. This is of course wrong, as electrons can come from ionizing HeI and HeII, but since He is 0.07 of the baryons, the error in this approximation is not large (but is significant). Also, accounting for He electrons would make Eq. (4) a coupled system between H and He; this would be ugly to solve. In addition, I assume that the HeI fraction is fixed at zero. Differing in notation from 16.56-16.58 in MvdBW, I arrive at the final expressions for the fraction of HI and HeII in the universe:

$$x_{HI} = (1 + A_i)^{-1} \quad (4)$$

$$x_{HeII} = (1 + 1/A_i)^{-1} \quad (5)$$

$$A_i = \frac{n_e \alpha_i(T)}{\Gamma_i} \quad (6)$$

where n_e is given in Eq. 3. Although the recombination rate coefficient is a function of temperature, I assume T is constant at the provided $2 \times 10^4 \text{ K}$. I take the coefficients using Case A from Draine's Eq. 14.5.

The results of this calculation are shown in Fig. 1, with the HI and HeII fractions shown in the solid and dashed lines respectively, the 1% line is drawn in blue, and the redshifts marking HI reionization and HeII reionization are shown in red dotted lines. HI is reionized at a $z=6.01$ and HeII at $z=4.08$.

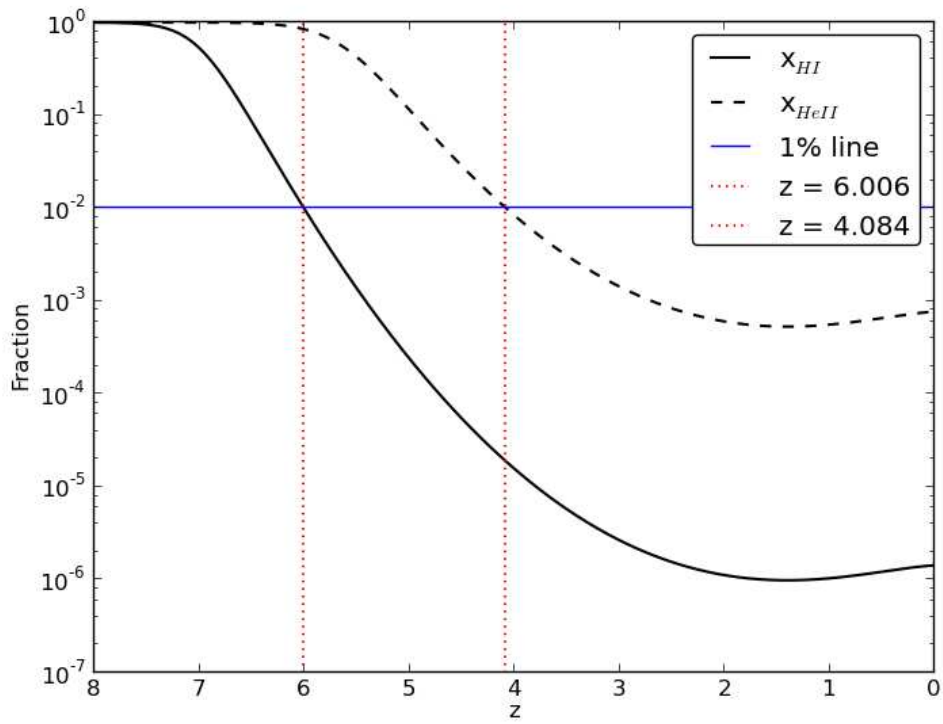


Figure 1: Plot of the evolution of the HI (solid) and HeII (dashed) fractions. The redshifts marking HI and HeII re-ionization are shown, and are defined as the point when the fractions dip below 1%.

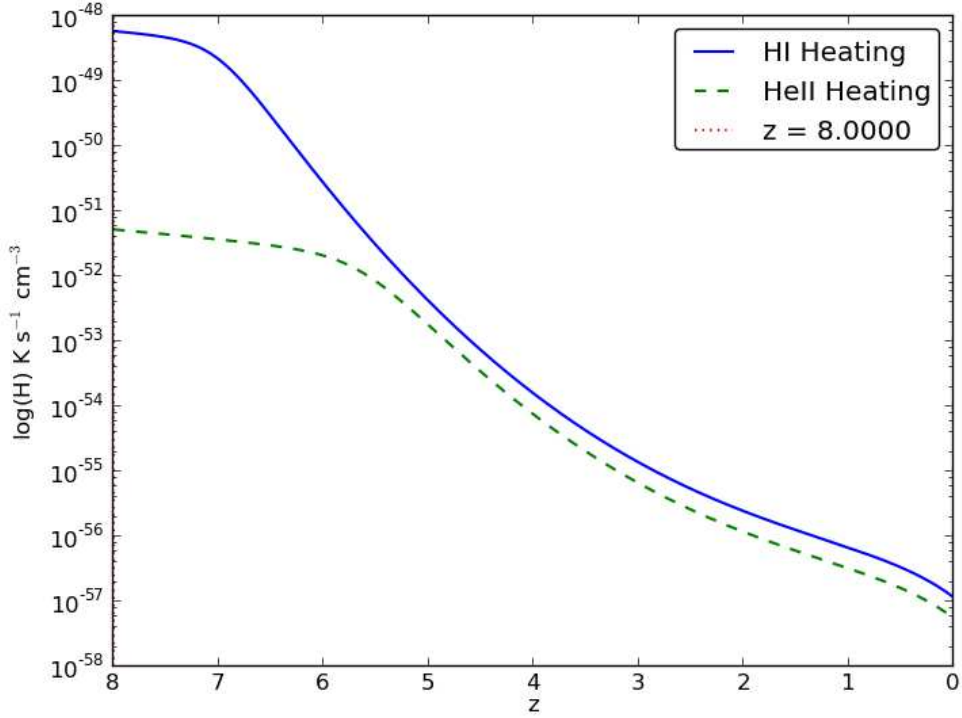


Figure 2: Heating rates per volume for both HI and HeII.

1.2 B and C.

The total heating rate per volume is given by equation 16.69 and 16.70 in MvdBW. Here we are just concerned with HI and HeII. The heating rate is then dependent upon the results from part A (as it depends upon the number density of the respective ions), so the assumptions made there extend here. Eq. 16.70 is long and I will not reproduce it here. I take $J(\nu)$ is taken as given in the problem, $\sigma_i(\nu)$ is the photionization cross section for the given ion, and is taken in full from Draine Eq. 13.1 and 13.2, and ν_i is the ionization frequency for the given ion. I integrate Eq. 16.70 of MvdBW numerically using SciPy's `integrate.quad` function, using the result to calculate the heating rate per volume. The actual number density of each ion is given by

$$n_{HI} = f_H x_{HI} n(z) \quad (7)$$

$$n_{HeII} = (1 - f_H) x_{HeII} n(z). \quad (8)$$

The fractions x_i are given by Eq. 4 and $n(z)$ is the given expansion evolution equation.

Fig. 2 gives the results of the calculation. As shown, HeII heating is always below HI. It becomes more significant, however, soon after HI is re-ionized. They appear to stay at roughly the same ratio for the rest of the evolution.

1.3 D.

At low redshifts, the thermal evolution of the IGM is going to be dominated by adiabatic cooling. The effects of cosmological expansion are still present, but heating/cooling due to the local density fluctuations will dominate. The temperature evolution will go as Eq. 4.25 in Chapter 4 of LF,

$$T \approx T_o (1 + \delta)^{\gamma-1}, \quad (9)$$

where $1+\delta$ reflects the local density ($\rho/\bar{\rho}$), γ is 1.6 at low redshift, and T_o is a normalization constant.

Other processes become relevant at higher gas densities, but this equation well approximates the general IGM temperature.

1.4 E.

Collisional processes (e.g. electrons colliding with hydrogen atoms) are able to heat and ionize a gas, and could conceivably be relevant for the IGM. However, the observed Ly α absorption by neutral gas in the IGM (the Ly α forest) indicates that this is not relevant. Ly α absorption features in the forest can be used as an indication of the thermal state of the IGM at a given redshift (the line width is affected in part by Doppler broadening, a thermal effect). Eq. 16.39 of MvdBW (kind of long, not going to type here) gives the equilibrium number density of neutral hydrogen in the IGM between ionization from collisional processes (electrons) and recombination. As discussed in MvdBW, in order to match with observations of the neutral HI via the Ly α forest, the temperature of the IGM must be above 10^6 K, which is inconsistent with observations. A typical doppler broadening value of the IGM in the forest is $b \sim 30$ km/s. Assuming only thermal contributions to b (i.e. ignoring turbulence, so $b = \sqrt{2 k_B T / m_H}$), this implies an upper limit on the typical IGM temperature as 5×10^4 K.

1.5 F.

The evolution of the brightness temperature of the 21-cm line is given in LF Chapter 12 as Eq. 12.8 (again, its long so I'm not going to retype it here). The a simulation of the evolution is plotted in Fig. 12.9 in the same chapter, and shows the effect of heating and photoionization on T_b . The brightness temperature is at a minimum at around $z \sim 20$. Since T_b is negative here, this implies the 21-cm signal can be seen in absorption. As discussed in LF, at this point the IGM begins to be heated significantly by the ionizing X-ray background formed by Population III stars, supernova remnants, stellar mass black holes, and quasars. After the significant X-ray heating, T_b reaches a maximum around $z \sim 15$ and 21-cm can be seen in emission. The effect of ionization on the IGM causes another turnaround shortly after this peak. After reionization begins, the brightness temperature begins to drop again, causing it to approach zero after reionization (by $z \sim 8$). In general, this was only a likely sketch of the actual evolution of T_b , which depends strongly on the models used.

2 3 Ionization and Diagnostics of Photoionized Regions

2.1 a) Strömgren spheres

Using Table 15.1 and equation 15.3, I calculated the HII ionization regions and the Strömgren radii for 5 O stars. For the radius of the HII regions obtained from cloudy, I used the condition given in the problem, where the ionization region is defined at $R(x_{HI} > 0.01)$. The results are tabulated in Table 2.1.

Star	Teff	qH	R_{HII}^a	R_{S0}^a	R_{HeII}/R_{HII}^b	R_{HeII}/R_{HII}^c
O3III	44540	49.77	3.44	3.23	0.959	1.04
O8III	33960	48.88	1.70	1.22	0.763	0.709
O4V	42860	49.44	2.63	2.38	0.935	1.03
O3I	42230	49.78	3.42	3.40	0.929	0.996
O8I	33180	49.25	2.28	1.63	0.749	0.732

^a Radii given in units of 10^{18} cm.

^b Calculated using Cloudy

^c Calculated using Eq. 15.36

For all stars, the actual (Cloudy) ionization regions are slightly larger than the Strömgren radii. The agreement is better for the hotter O stars, and worse for the cooler O stars. This is because as qH increases, the ionization region becomes better approximated by a Strömgren Sphere. The approximation as a Strömgren Sphere improves for larger qH because the mean free path of an ionizing photon (Eq. 15.5) becomes smaller relative to R_{S0} ($mfp \ll R_{S0}$), since R_{S0} increases with increasing qH . Since a Strömgren Sphere assumes a discontinuous boundary between ionized and neutral gas, the boundary region becomes smaller (approached 0, i.e. is discontinuous) as R_{S0} increases.

2.2 b) Radii of He II vs H II zones:

I define the HeII region as that where $x_{HeI} > 0.1$, as was done for HII above. To compare the results to Eq. 15.36, I assume $y = 0.2$ and $z = 0.8$ as done in the book in Sec. 15.5. The $\alpha_B(H)$, $\alpha_{1s}(He)$ $\alpha_B(He)$ values are taken from Table 14.1, Eq. 14.14, and Eq. 14.15 respectively; all three are a function of temperature. $n_H = 10^3$ is taken from the model, and n_{He} is obtained using the defined abundance of He relative to H given in the model. The results are shown in the last two columns of Table 2.1. The differences between the Cloudy results and the analytic calculation are not too bad, within 8.4%, 7.0%, 10.2%, 7.2%, and 2.3% for each star respectively. The errors are most likely due to the assumptions made on y and z .

2.3 c) Temperature diagnostics:

The volume integrated emissivities (i.e. the line strengths) for the 5007Å and 4363Å lines of OIII are obtained from the model and are tabulated for each star in Table 2.3. Included also is the diagnostic ratio of the 4363Å to 5007Å line, and the average electron temperature in the nebula. Comparing this to Fig. 18.2, the results agree well (assuming $n_e < 10^3$). Each star has a ratio between $\sim 2.0 \times 10^{-3}$, which indicates an electron temperature of around 8×10^3 K. This agrees with the actual averaged electron temperature.

Star	OIII 5007Å / 10^{37} ^a	OIII 4363Å / 10^{34} ^a	Ratio/ 10^{-3}	$\langle T_e \rangle / 10^3 \text{ K}$
O3III	12.0	38.0	3.17	8.67
O8III	0.378	0.776	2.05	7.47
O4V	4.43	12.8	2.88	8.34
O3I	9.57	26.9	2.81	8.40
O8I	0.841	1.67	1.98	7.46

2.4 d) Density Diagnostics:

The electron density varies most dramatically towards larger radii. More specifically, the density decreases dramatically through the boundary between the ionization and neutral regions, out to the edge of the system. The dramatic increase in the last couple of percent of the normalized radius indicates a fairly sharp transition region from ionized to neutral.

The low density limit in Eq. 18.5 has a temperature dependence on the rate coefficients (Ω_{ul}) as given in Table F.5. For the temperature in this equation, I use the temperature at the region where the number density of electrons is a minimum (NOTE: with the ratio, the temperature dependence is very weak, so this doesn't really matter much). The high density limit is given by Eq. 18.6, with constants g_2 and g_1 obtained from Fig. 18.3, and $A_{20} = 1.88 \times 10^{-4} \text{ s}^{-1}$ $A_{10} = 5.63 \times 10^{-4} \text{ s}^{-1}$ obtained from the NIST table. Fig. 3 gives an example of the density diagnostic for an O3I star with the lower and upper density limits plotted at a line ratio of 1.50 and 0.50 respectively. The actual ratio of the nebula's emission is within these bounds for all stars. The transition point occurs at an electron density of around 10^3 cm^{-3} for each star (I just eyeballed this from the plots).

2.5 e) BPT Diagram:

The BPT diagram for all stars is shown in Fig. 4. As shown, the stars occur on the BPT diagram in order of temperature/qH (hottest at the top, coolest at the bottom). This implies that as qH increases, the corresponding nebula shifts up and to the right on the BPT diagram. This means both the NII and OIII lines become stronger, relative to $H\alpha$ and $H\beta$ respectively, as qH increases. Tracking the 80% region, (NOTE: I'm using a different colormap, but 80% is still orange in my case), it appears on the horizontal portion (lower NII/ $H\alpha$, higher OIII/ $H\beta$) for the hotter stars (O3III, O3I, and O4V in this case), and is more on the vertical portion (higher NII/ $H\alpha$, lower OIII/ $H\beta$) for the cooler stars (O8III and O8I).

One could use this trend to, in principle, pick out the relative ages of galaxies and learn something about their star formation. Galaxies appearing towards the right (more vertical) side of the figure will have cooler, older O stars, while galaxies appearing up and towards the left (horizontal) will have hotter, younger O stars. In the latter, then, star formation was more recent.

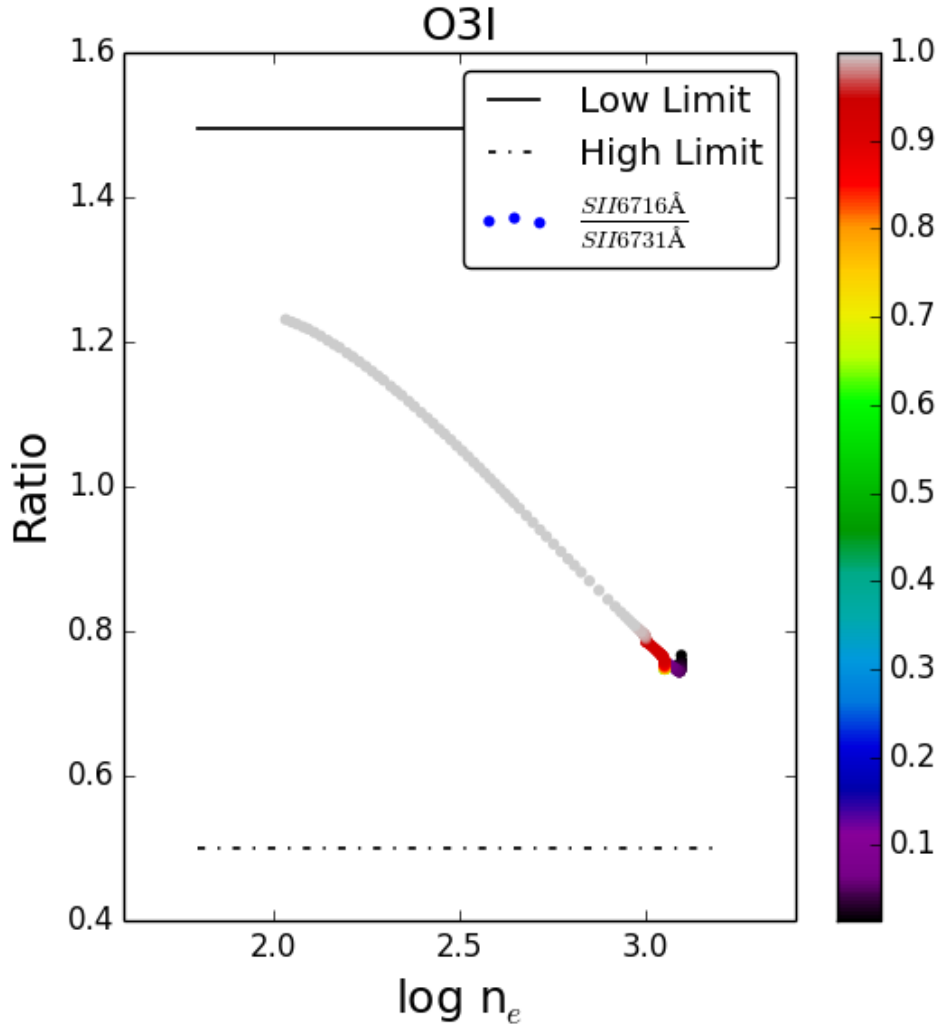


Figure 3: Density diagnostic for an O3I star with plotted low and high density limits on the ratio. The Cloudy ratio is between these bounds.

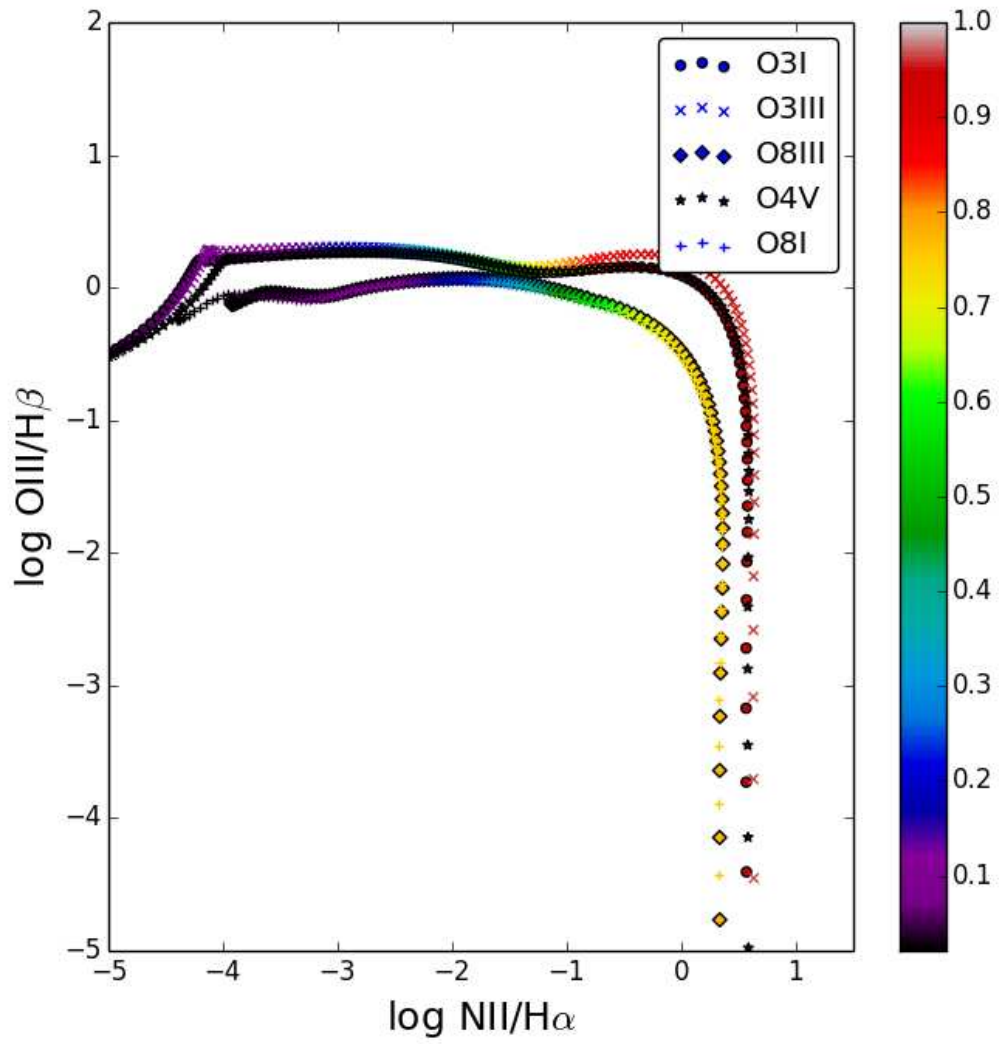


Figure 4: BPT Diagram for all 5 O stars. The plus signs represent the O8I star, and are hard to see, but are lined up roughly with the diamonds from the O8III star

2.6 f) Metallicity variations:

Decreasing the metallicity has two immediately obvious effects on the electron temperature in the nebula. The first, is that it raises the overall electron temperature for the entire nebula. Eyeballing averages from the graphs, the average temperature (given as T_4) increases from around 1.1 to 1.8 between the 0.3 and 0.01 metallicity values. The second effect is to smooth out the overall temperature, removing peaks at larger radii. In addition, there is a noticeable depression in the temperature in the ionized region for the 0.3 case, that is gone in the 0.01 case (roughly linear).

A lower metallicity implies that more high energy ionizing photons (above Helium's ionization energy) are available (there are less metals to absorb them). This increases the chances that one of these higher energy photons will ionize Hydrogen, imparting a larger kinetic energy on the ejected electron, raising the electron temperature.

The ratio of the OIII 4346Å line to the OIII 5007Å line in the temperature diagnostic increases with decreasing metallicity. Assuming roughly constant electron densities between the three cases (for comparisons sake), which is fine if n_e is below 1000 cm^{-3} , an increase in the ratio implies a hotter medium, which is the case. The average electron temperature increases with decreasing metallicity, from $1.0 \times 10^4 \text{ K}$ to $1.5 \times 10^4 \text{ K}$ between the 0.3 to 0.01 cases.

The emissivities all decrease as metallicity decreases ($H\beta$ has the smallest change). For the 0.01 metallicity case, the SII and NII emissivities become very small at all radii. OIII is now below $H\beta$ and $H\alpha$ at all radii (not the case for 0.3 metallicity). $H\alpha$ is dominant at the lower metallicity. Though the total emissivity decreases for all lines, the ratio of $H\alpha$ to $H\beta$ appears to be approximately the same across metallicity.